Romanian Reports in Physics **71**, 502 (2019)

CHARACTERIZATION OF PRECIPITATION IN 2000 SERIES ALUMINIUM ALLOYS USING NEUTRON DIFFRACTION, SANS AND SEM METHODS

GIZO BOKUCHAVA[1,*], YULIA GORSHKOVA[1], RICARDO FERNÁNDEZ[2], GASPAR GONZÁLEZ-DONCEL[2], GIOVANNI BRUNO[3]

[1] Joint Institute for Nuclear Research, Frank Laboratory of Neutron Physics, Joliot-Curie Str. 6, 141980 Dubna, Russia
[*] Corresponding author, E-mail: gizo@nf.jinr.ru; E-mail: gorshk@nf.jinr.ru
[2] Centro Nacional de Investigaciones Metalúrgicas (CENIM), Department of Physical Metallurgy, C.S.I.C., Av. de Gregorio del Amo 8, E-28040 Madrid, Spain
E-mails: ric@cenim.csic.es, ggd@cenim.csic.es
[3] Federal Institute of Materials Research – BAM, Unter den Eichen 87, 12205 Berlin, Germany
E-mail: giovanni.bruno@bam.de

Received December 4, 2017

Abstract. Combination of high-resolution time-of-flight (TOF) neutron diffraction, scanning electron microscopy (SEM) and small angle neutron scattering (SANS) have been used to study hardening precipitation in 2014Al and 2124Al alloys. Neutron diffraction experiment revealed presence of tetragonal $CuAl_2$ phase (θ/θ′ precipitates) in 2014Al alloy and orthorhombic $CuMgAl_2$ phase (S-precipitates) in 2124Al alloy. SEM image analysis revealed that the θ/θ′-precipitates have platelet morphology while the S-precipitates exhibit rod-like shapes. From SANS data analysis the characteristic dimensions of precipitate particles and their polydisperse distributions were estimated.

Key words: neutron diffraction, small angle neutron scattering, scanning electron microscopy, precipitation hardening

1. INTRODUCTION

Aluminum alloys of 2xxx series are widely used in aerospace industry at room temperature for their high mechanical strength. However, in the range of temperatures above 400 K, their mechanical performance decrease due to overaging precipitation processes. The creep behavior of aluminum and its Al-Cu alloys processed by ingot metallurgy has been extensively investigated [1–14]. In the range of high temperatures, the creep activation energy of the process for pure aluminum was identified to the aluminum self-diffusion energy = 142 kJ / mol [15, 16]. This reveals that vacancy diffusion is a key factor in the creep phenomenon as the rate controlling process of dislocation motion through a dislocation-climb mechanism. However, for age-hardenable alloys, a universally accepted value of the activation energy for the creep process is not available. Moreover, very different stress

exponents (n) in the power law creep are found. This is due, in part, to the facts that creep tests are commonly carried out at temperatures at which precipitation in age-hardenable alloys evolves depending on the test conditions [17]. Dislocation dynamics is also influenced by alloying elements involved in the precipitation process [18]. Precipitation plays a crucial role in the creep behavior of these alloys [19, 20]. It is clear that the influence of precipitation during the creep test must be characterized for a rigorous analysis of the creep data at different temperatures. However, solid-state precipitation is barely considered in the literature [11]. In fact, little agreement is found in the literature on the mechanisms that governs the creep of Al-Cu alloys [12–14]. On the contrary, the precipitation sequence in Al-Cu-Mg-Si-Mn alloys is well established [21–23] and its dependence on the phenomenon dependence on testing conditions (temperature and stress) among others has been extensively studied. The precipitation process occurring in 2xxx aluminum series alloys are related to Cu, Mg and Si elements. The chemical composition of the alloy greatly influences the evolution of precipitates composition during ageing at moderated temperatures (< 550 K). In particular, two main precipitation sequences have been described depending on the Mg content of the alloy. Alloys with low Mg content present $CuAl_2$ precipitates meanwhile alloys with high Mg content present $CuMgAl_2$ precipitates (see, for example, [21, 23]).

Then, it has been determined that the kinetics of this precipitation sequence is strongly dependent on temperature and stress among other factors has been extensively studied [24]. For example, an over-aged condition, θ-precipitates, is achieved at three hours of thermal treatment at 453 K. With further annealing time, precipitates coarsening (Ostwald ripening), occurs. Even in this over-aged condition, alloying elements produce a strengthening effect with respect to pure aluminum in creep conditions [1]. The two main strengthening contributions come from the solid solution and coherent precipitates present in the alloys. The strengthening effect is strongly dependent on the heat treatment suffered by the alloys. In the present research, we study the effect of exposure to creep conditions on the precipitation sequence in 2014 and 2124Al alloys by means of TOF neutron diffraction, SEM and SANS. Thereby, the lattice parameter under different exposure times at 473K is determined, and both precipitate and coherent precipitates size distributions are calculated under the same conditions.

2. MATERIALS AND EXPERIMENTS

In this research, two series of 2014Al and 2124Al aluminum alloy powders, which respective chemical compositions are shown in Table 1, were investigated. As it can be seen from this table, Si and Mg are the elements whose contents are significantly different from one alloy to the other. The samples were subjected to different heat treatment durations (t = 0, 0.3, 1, 3, 10 and 100 hours) at temperature T = 200°C.

Table 1

Chemical composition of 2014Al and 2124Al alloys

Element / Alloy	Si	Fe	Cu	Mn	Mg	Cr	Zn	Ti
2014Al	0.72 ± 0.01	0.083 ± 0.002	4.40 ± 0.10	0.012	0.52 ± 0.01	<0.002	<0.005	<0.05
2124Al	0.113 ± 0.005	0.104 ± 0.002	4.17 ± 0.05	0.59 ± 0.01	1.50 ± 0.01	<0.002	0.011	<0.05

For evaluation of main structural parameters of crystalline phases in Al alloys high-resolution time-of-flight (TOF) neutron diffraction have been used. SEM method allowed to detect the presence of precipitate particles and to characterize their morphology. SANS method have been used to estimate typical dimensions of coherent precipitates and their variation with heat treatment duration.

The neutron TOF diffraction experiments have been performed on Fourier stress diffractometer FSD at the IBR-2 fast pulsed reactor in FLNP JINR (Dubna, Russia) [25, 26]. The FSD diffractometer was specially designed for residual stress studies in bulk industrial components and new advanced materials [27]. On FSD, a special purpose correlation technique is used to achieve high resolution level of the diffractometer – a combination of the fast Fourier chopper for the primary neutron beam intensity modulation and the reverse TOF method for data acquisition [28, 29]. This makes it possible to obtain high-resolution neutron diffraction spectra $\Delta d/d \approx 2 \cdot 10^{-3}$ for backscattering detector ($2\theta = 140°$) and $\Delta d/d \approx 4 \cdot 10^{-3}$ for ±90° – detectors at $d = 2$ Å with the fairly short flight distance (~6.6 m) between Fourier chopper and neutron detectors.

SANS experiments have been performed on the YuMO neutron small-angle spectrometer at the IBR-2 reactor in FLNP JINR (Dubna, Russia) [30]. The instrument is designed to study materials structure in nanoscale range. YuMO is characterized by a high neutron flux (2×10^7 n/cm^2/s) and a wide range of transmitted momentum $Q = 0.007 \div 0.5$ Å^{-1}.

3. NEUTRON DIFFRACTION ANALYSIS

As a rule, TOF diffractometers exhibit a rather wide range of interplanar spacing and, consequently, possess a large number of simultaneously observed diffraction peaks with the almost similar contribution of the resolution function to their widths. In addition, the functional dependence between the diffraction peak width and the interplanar spacing enables one to estimate microstrain and the size of coherently scattering domains (crystallites) in a rather simple way [31, 32]. In scale of interplanar spacing d_{hkl} the resolution function of the neutron TOF diffractometer is defined by the expression

$$R = \Delta d/d = [(\Delta t_0/t)^2 + (\Delta\theta/\mathrm{tg}\theta)^2 + (\Delta L/L)^2]^{1/2}, \quad (1)$$

where Δt_0 is the neutron pulse width, $t = 252.778 \cdot L \cdot \lambda$ is the total time of flight (in microseconds), L is the total flight distance from a neutron source to detector (in meters), λ is the neutron wavelength (in Å). The first term is the time component of the resolution function, *i.e.*, a TOF uncertainty; the second is the geometric component of the resolution function, which characterizes all geometric uncertainties during scattering at different angles; and the third is a flight path uncertainty.

From Eq. (1) it follows that the width of the individual diffraction peak as a function of the interplanar spacing d_{hkl} can be written in the following form

$$\Delta d^2 = C_1 + C_2 \cdot d^2, \tag{2}$$

where C_1 and C_2 are some constants related with Δt_0 and $\Delta\theta$, respectively, *i.e.* the time and geometric components of the diffractometer resolution function. A routine method for determining these values is a diffraction experiment with standard specimen, which assumes no microstrain and rather large crystallites.

According to Williamson-Hall analysis for real crystals the diffraction peak broadening effect due to the presence of microstrain ε and finite crystallite size $\langle D \rangle$ is expressed by the formula

$$\beta^2 = (2 \cdot \varepsilon \cdot d)^2 + (k \cdot d^2/\langle D \rangle)^2, \tag{3}$$

where a Gaussian approximation for distribution functions is assumed, $\varepsilon = \Delta a/a$ is the variance of the unit cell parameter (microstrain), $\langle D \rangle$ is the average size of crystallites, k is a dimensionless coefficient close to unity which takes into account the shape of crystallites. Combining the expressions for Δd^2 and β^2 the diffraction peak width at half maxima as a function of interplanar spacing d can be obtained as

$$\Delta d^2 = C_1 + C_2 \cdot d^2 + C_3 \cdot d^2 + C_4 \cdot d^4, \tag{4}$$

where $C_3 \approx (2 \cdot \varepsilon)^2$ and $C_4 \approx (k/\langle D \rangle)^2$ are contributions to the diffraction peak broadening due to microstrain and finite crystallite size, correspondingly. The dependences $\Delta d^2(d^2)$ will be linear with higher slope as compared to standard specimen if the peak broadening is caused by the presence of microstrain only and finite crystallite size effect is negligible (large crystallites). In case of small crystallites, the peak broadening due to size effect is well pronounced and gives characteristic parabolic dependence. Accordingly, plotting these dependences in a sufficiently large range of d_{hkl}, one can easily separate contributions to diffraction peak broadening due to microstrain ε and finite crystallite size $\langle D \rangle$ and determine these microstructural parameters independently [33].

Additionally, the average lattice microstrain can be estimated from diffraction peak width parameter *W1* obtained from Rietveld fit [34] of TOF neutron diffraction data. In this case, the general formula for width of diffraction peaks measured with Fourier diffractometer is:

$$W^2 = W_{\mathrm{TOF}}{}^2 + W1^2 \cdot d^2 + W2^2 \cdot d^4 = W_{\mathrm{TOF}}{}^2 + (W_{\mathrm{ang}}{}^2 + W_{\mathrm{strain}}{}^2) \cdot d^2, \tag{5}$$

where $W_{TOF} \sim 1/V_{max}$ is the time contribution to the resolution function defined by maximal Fourier chopper speed V_{max} during measurement, $W_{ang} \sim \Delta\theta/tg\theta$ is geometrical contribution to resolution function and W_{strain} is peak broadening contribution due to microstrain.

4. RESULTS AND DISCUSSION

4.1. NEUTRON DIFFRACTION

During the experiment on the FSD diffraction spectra from Al alloy powder samples of the both series are measured at room temperature in standard Ø8 mm vanadium containers. All main diffraction peaks from Al phase are indexed in the frame of the cubic FCC structure (sp. gr. *Fm*3*m*) with lattice constant $a \approx 4.047$ Å. In addition to the main Al phase, the measured TOF spectra also exhibited weak peaks from the precipitate phases with roughly constant peak intensities, which indicate an almost constant volume content of these phases during heat treatment. The precipitate phases present even in T4 (initial) samples for both alloy series. For 2014Al alloy the additional phase was identified as θ/θ′ precipitates of the tetragonal $CuAl_2$ phase (sp. gr. *I4/mcm*) with lattice constants $a \approx 6.0748$ Å, $c \approx 4.8831$ Å. In 2124Al alloy S-precipitates of the orthorhombic $CuMgAl_2$ phase (sp. gr. *Cmcm*) with lattice constants $a \approx 4.011$ Å, $b \approx 9.251$ Å, $c \approx = 7.152$ Å are observed (Fig. 1). These results are in good agreement with previously observed phase compositions [35].

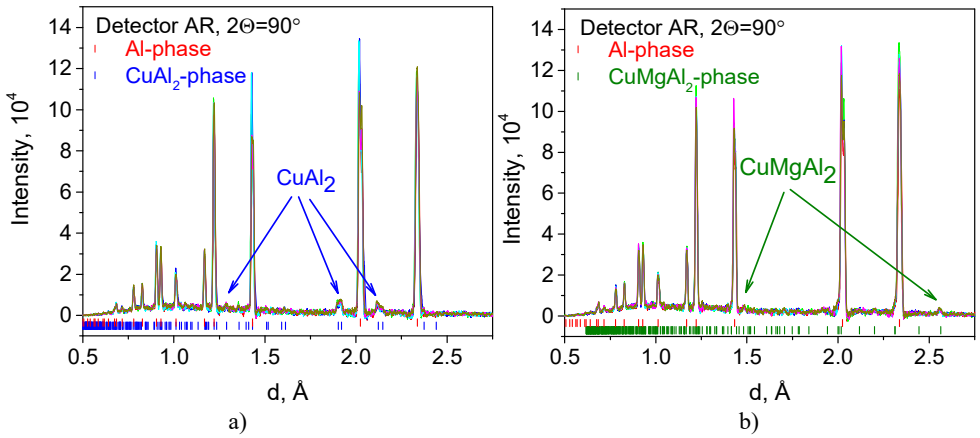

Fig. 1 – Neutron diffraction spectra from 2014Al (a) and 2124Al (b) alloys. Strongest peaks from tetragonal $CuAl_2$ (θ/θ′ precipitates) and orthorhombic $CuMgAl_2$ (S-precipitates) phases are visible.

The measured diffraction spectra were processed using full profile analysis based on the Rietveld method and main structural parameters for Al phase are obtained. It was found that, depending on the heat treatment duration *t*, there is a

noticeable variation in the lattice constants and the peak width parameters, which is apparently due to the formation of precipitates in the material (Fig. 2). The study of diffraction peak broadening demonstrated that crystallite sizes contribute negligibly to the peak broadening. On the contrary, microstrains make the main contribution to the above phenomenon.

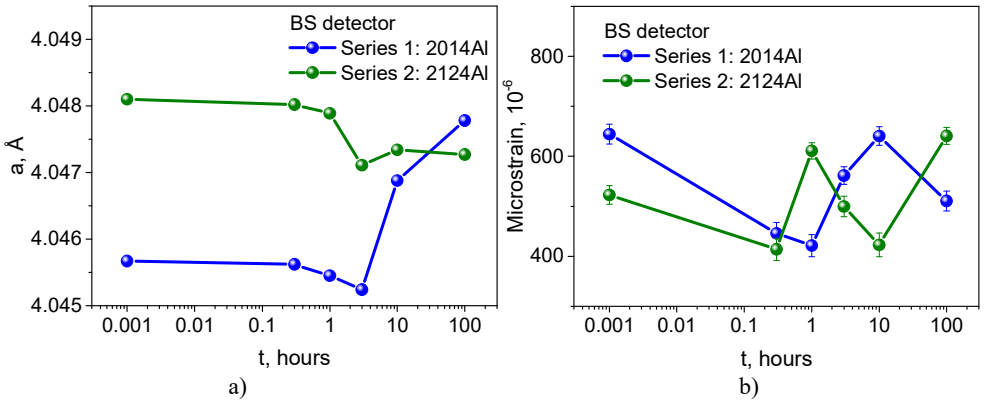

Fig. 2 – Lattice parameter (a) and microstrain (b) for Al-phase obtained from the Rietveld fits of neutron diffraction spectra.

4.2. SCANNING ELECTRON MICROSCOPY

The precipitation state for 3 h and 100 h of 2014 and 2124 alloys is shown in Fig. 3a, b. The appearance of the aluminum powder particles at low magnification is characterized by the presence of very big incoherent precipitates (> 500 nm). These big precipitates, characterized as Al-Cu using the EDAX analysis of the SEM, are typical of an over aged state, and are present both for the 3 h and 100 h samples in the 2014Al and the 2124Al alloys. This result indicates that the solubilization process of the aluminum powders was not completed. The solubilization and quenching process of 2xxx series aluminum powders is a very complex task due to the special thermal behavior of the Al-Cu system; even when small particle size powders are used. As it is shown in Fig. 3b, the same heat treatment can induce very different precipitation state for every individual powder particle. For example, the particle located in the lower position of Fig. 3b (delimited by a green line), presents almost twice the number of precipitates per unit area (white dots) than the particle located in the upper position (delimited by the blue line). This effect can't be related to either the solubilization + quenching step or to the ageing treatment. These differences must be mainly related with the aluminum powder particle localization into the container used for the solubilization + quenching step. Those particles that were located close to the container wall during the solubilization + quenching step will present a more pronounced precipitation state. Apart from the

big (> 500 nm) precipitates, a small population of small size precipitates are present in the all the samples studied.

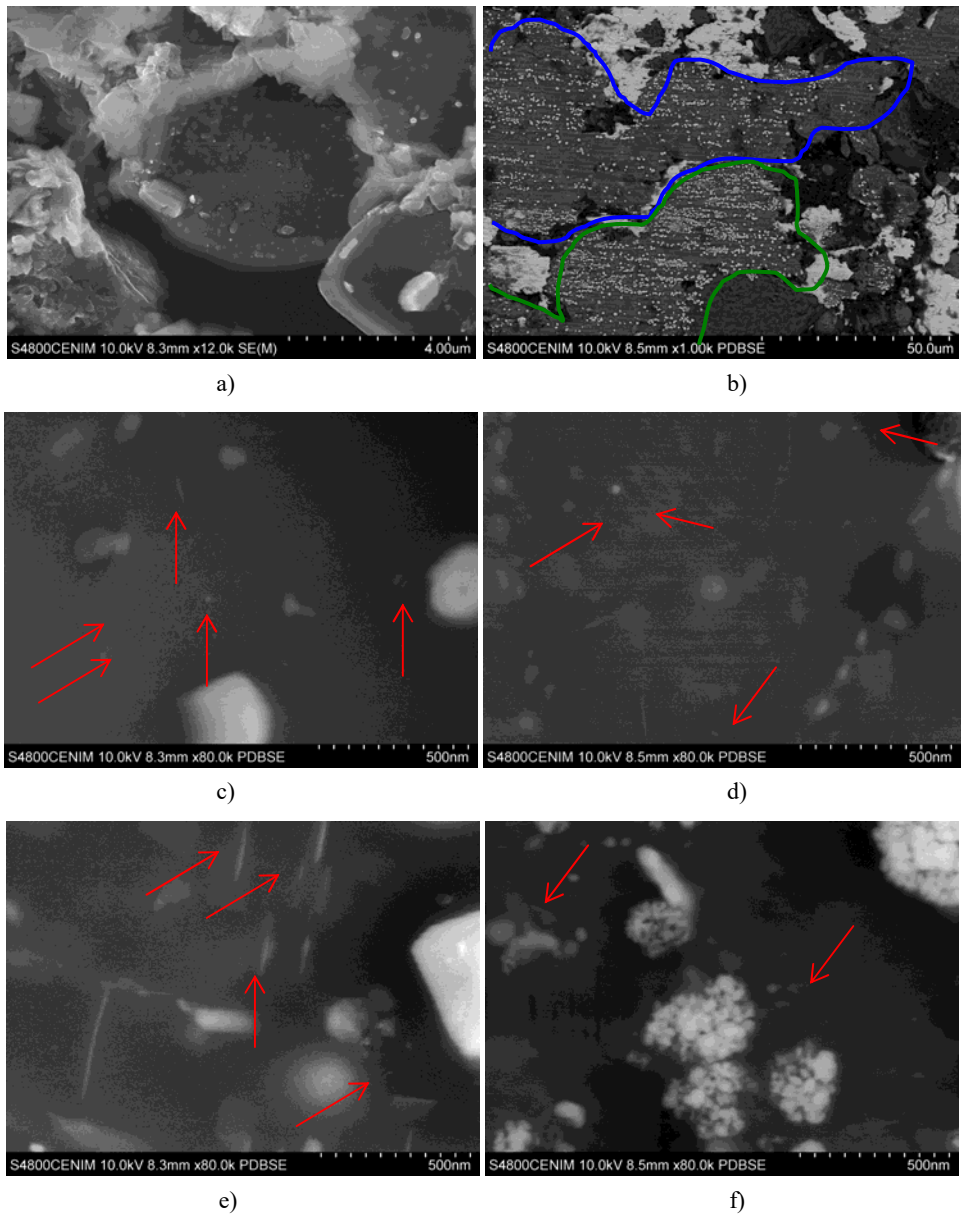

Fig. 3 – a) Typical appearance of a) 2014Al and b) 2124Al (100 h) powder particles at low magnification. White particles are big precipitates. c) and d) Small precipitates (indicated by red arrows) for 2014Al and 2124Al (3 h), respectively. e) and f) Small precipitates details for 2014Al and 2124Al (100 h), respectively.

The SEM analysis confirmed high-aspect-ratio platelet morphology for θ/θ′-precipitates in 2014Al alloy while S-precipitates in 2124Al alloy exhibit rod-like morphology. The main difference between small precipitate populations of 3h and 100h samples is that 100h samples present an increased precipitates density. On the other hand, there is a very important difference between 100h samples of the 2014Al and 2124Al alloys. In the 2014Al alloy the small precipitates are dispersed into the aluminum matrix. However, in the 2124Al alloy, a high degree of precipitates agglomeration can be observed at high magnification. In fact these agglomerates of precipitates resemble big precipitates at low magnification.

In addition, the SEM data indicate that the both type precipitates are not monodisperse. For this reason, polydispersity in precipitate dimensions distribution should be considered in SANS data analysis.

4.3. SMALL-ANGLE NEUTRON SCATTERING

During SANS experiments Al alloy powder samples of the both studied series were placed into a 1 mm thick quartz cuvette. All measurements are performed at room temperature. Two ring wire He^3-detectors at distances of 4 m and 13 m from the sample position were used in our experiment. The scattered intensity (differential cross section per sample volume) is registered as a function of the momentum transfer modulus $Q = (4\pi/\lambda)\sin(\theta/2)$, where θ is the scattering angle and λ is the incident neutron wavelength. An incident neutron beam distribution provides an available wavelength range of $0.5 \div 8$ Å, which corresponds to momentum transfer range Q of $0.0068 \div 0.54$ Å^{-1}. The measured SANS spectra are converted to the absolute scale by normalization to the incoherent scattering cross section of standard vanadium sample (Fig. 4) and corrected for scattering from the setup and empty cuvette.

The SANS curves are fitted by function consisting of two terms. The first term is a Porod-type contribution in the low-Q region corresponding to power-law scattering from sharp boundaries of large-scale objects (coarse precipitates, grain boundaries, dislocations, etc.). The second one corresponds to scattering from precipitate particles, which can be described by the form factor of a cylinder with radius R, and length L [36, 37]:

$$I(Q) = AQ^{-4} + N(\Delta\rho)^2 V^2 \left(\frac{\sin(QL\cos(\alpha)/2)}{QL\cos(\alpha)/2} \right)^2 \left(\frac{2J_1(QR\sin(\alpha))}{QR\sin(\alpha)} \right)^2 + C, \quad (6)$$

where A is a constant, N is the particle number density, V is the volume of a single precipitate, α is the angle between cylinder axis and Q vector, Δρ (contrast) is the scattering length density difference between the matrix and the precipitates, J_1 is the first order Bessel function and C is the incoherent background.

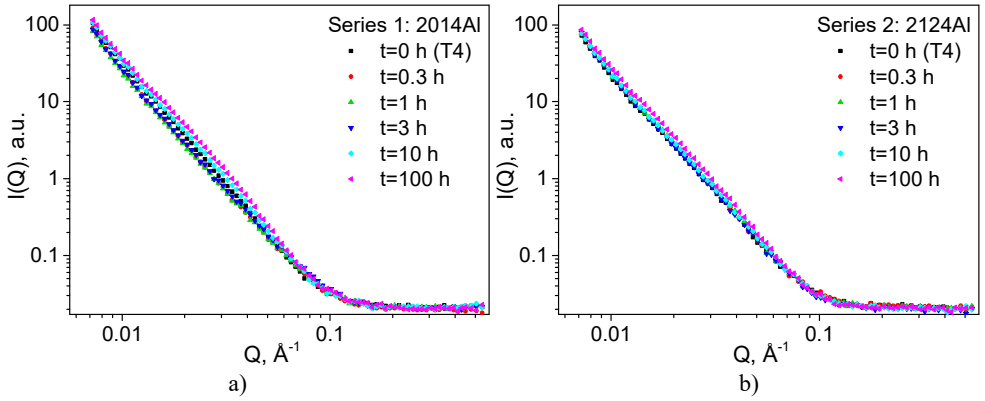

Fig. 4 – Evolution of experimental SANS curves for 2014Al (a) and 2124Al (b) alloys with increase of heat treatment duration.

The experimental SANS data are fitted with SasView software [38] using described model. The different particle shapes are used to describe the precipitate scattering contribution to the total SANS intensity: platelet ($L << R$) shape particles for θ/θ′ precipitates in 2014Al alloy series samples and rod ($L >> R$) shape particles for S precipitates in 2124Al alloy series samples (Fig. 5). In accordance with the generally accepted approach [39, 40] a lognormal distribution of the cylinder radius and length is used in the model for the correct consideration of the polydispersity of the system and relevant fit of SANS profiles.

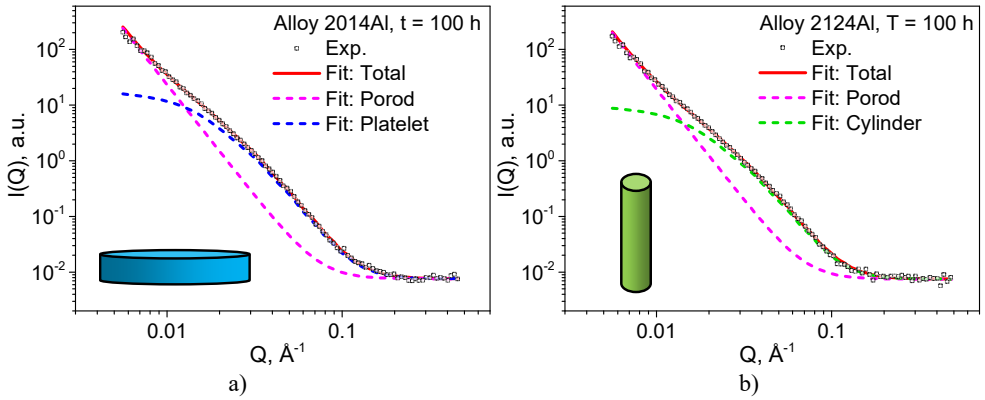

Fig. 5 – Examples of SANS data fits using different particle models: platelet shape for 2014Al alloy (a), rod shape for 2124Al alloy (b).

The structural parameters extracted by model are presented in Figs. 6 and 7. Dimensions of platelet shape θ/θ′ precipitates in 2014Al alloy are within the following ranges: R = 132 ÷ 150 Å and L = 33 ÷ 50 Å. For cylindrical shape S precipitates in 2124Al alloy typical dimensions are R = 19 ÷ 22 Å and L = 267 ÷ 299 Å. It should

be noted that precipitate particles in both alloys exhibit rather moderate dynamics, which can be explained by overaged state of the material. The polydispersity of particle radius determined by SANS analysis is estimated as 0.2–0.38 for 2014Al alloy and it exhibit higher values of 0.63–0.66 for 2124Al alloy.

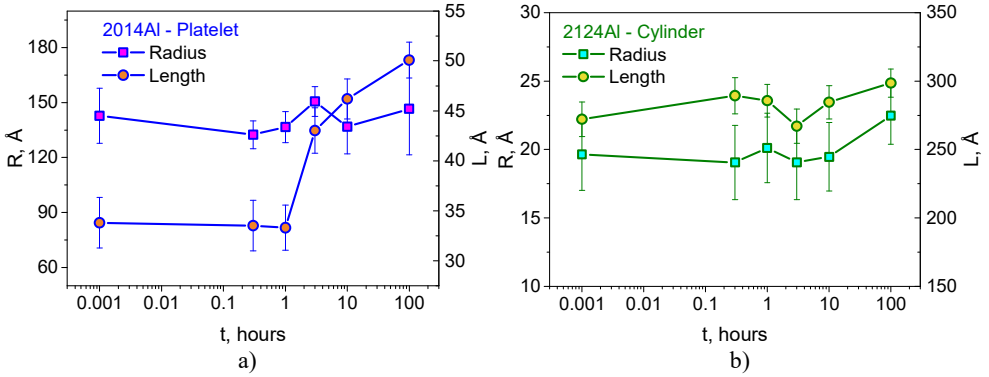

Fig. 6 – Radius and length of precipitate particles *vs*. heat treatment duration for alloys 2014Al (a) and 2124Al (b).

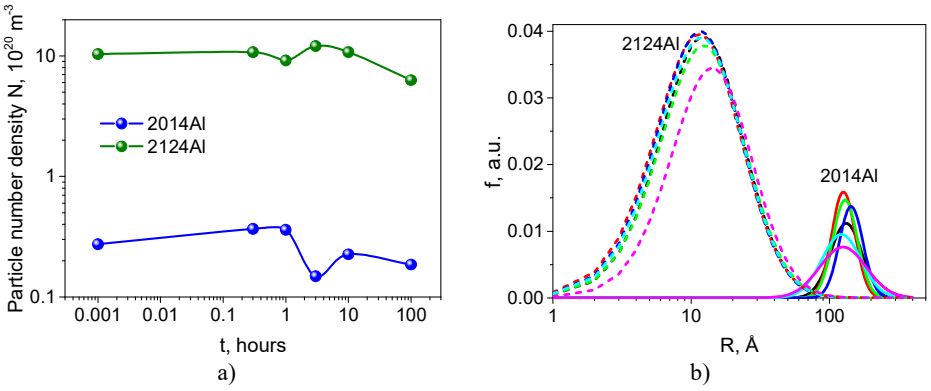

Fig. 7 – a) Precipitate particle number density; b) radius distribution functions of precipitates.

5. CONCLUSIONS

The complementary methods of TOF neutron diffraction, SEM and SANS were used to study the relationship between phase compositions and structural parameters of precipitate phases in 2014Al and 2124Al alloys. Neutron diffraction reveals clearly the presence of crystalline phases of precipitates, which are responsible for noticeable variation in the lattice parameter and lattice microstrain values. The analysis of SEM images has confirmed the presence of nanoscale precipitate particles and characterized their shapes and approximate dimensions. Additionally, the SEM

characterization has shown big differences in the precipitation state of aluminum powder particles for a given heat treatment. This result is mainly related with the distance to the container wall (affecting the quenching step) of every individual aluminum powder particle. There are also differences in the volume fraction of small (< 20 nm) precipitates among the samples studied (Table 2).

Table 2

Volume fraction of precipitates estimated from SEM data. A typical error is around 0.02%

Alloy	Heat treatment	Volume of precipitates (%)
2014Al	3 h	0.2
	100 h	2.0
2124Al	3 h	0.1
	100 h	Agglomerates

The SANS data have provided details of the change in dimensions, volume fraction and polydispersity of precipitate particles during ageing. The obtained information is useful for better understanding of complex phenomena in nanoscale precipitation processes and development of theoretical models. Thus, the present work demonstrates the potentialities of combination of these experimental techniques for deep investigation of phase interactions in modern lightweight materials.

Acknowledgements. G. Bokuchava and J. Gorshkova acknowledge support within the Romania-JINR Programme 2017 and from Russian Foundation for Basic Research (project No. 15-08-06418_a). R. Fernández and G. González-Doncel are grateful to the financial support of project MAT2014-55415-C3-1R (Spain) and the beamtime from FLNP JINR (Dubna, Russia).

REFERENCES

1. I.S. Servi and N.J. Grant, Trans. AIME, **191**, 909–916 (1951).
2. I.S. Servi and N.J. Grant, Trans. AIME, **191**, 917–922 (1951).
3. L. Chen, G. Zhao, J. Gong, X. Chen, M. Chen, J. of Mat. Eng. and Perf., **24**(*12*), 5002–5012 (2015). http://doi.org/10.1007/s11665-015-1734-4
4. Y.C. Lin, Qi-Fei Li, Yu-Chi Xia, Lei-Ting Li, Mat. Sci. Eng. A **534**, 654–662 (2012). https://doi.org/10.1016/j.msea.2011.12.023
5. E. Gariboldi, F. Casaro, Mat. Sci. Eng. A **462**, 384–388 (2007). https://doi.org/10.1016/j.msea.2006.04.153
6. L. Mordfin, N. Halsey, P.J. Granum, National Bureau of Standards. Technical note 55 (1960).
7. E.E. Mathauser and W.D. Deveikis, National advisory committee for aeronautics. Report 1308 (1957).
8. Z.Y. Ma, S.C. Tjong, Comp. Sci. and Tech. **59**, 737–747 (1999). https://doi.org/10.1016/S0266-3538(98)00113-4.
9. K.M.B. Tamminger, *Analysis of creep behavior and parametric models for 2124Al and 2124-SiCw composite*, PhD Thesis, Virginia Polytechnic Institute and State University, 1999.
10. S. Banerjee, P.S. Robi, A. Srinivasan, L. P. Kumar, Mat. Sci. Eng. A **527**, 2498–2503 (2010). https://doi.org/10.1016/j.msea.2010.01.052.
11. T.J. Smith, H.J. Maier, H. Sehitoglu, E. Fleury, J. Allison, Met. and Mat. Transactions A **30**, 33–146 (1999). https://doi.org/10.1007/s11661-999-0201-y.
12. Y.C. Lin, L.T. Li, Y.C. Xia, Comput. Mater. Sci. **50**, 2038–2043 (2011). https://doi.org/10.1016/j.commatsci.2011.02.004.

13. G.R. Ebrahimi, A. Zarei-Hanzaki, M. Haghshenas, H. Arabshahi, J. Mater. Process. Tech. **206**, 25–29 (2008). https://doi.org/10.1016/j.jmatprotec.2007.11.261.
14. R. Lapovok, C. Loader, F.H. Dalla Torre, S.L. Semiatin, Mat. Sci. Eng. A **425**, 36–46 (2006). https://doi.org/10.1016/j.msea.2006.03.023.
15. O. D. Sherby, P. M. Burke, Prog. In Mat. Sci., **13**, 323–390 (1968). https://doi.org/10.1016/0079-6425(68)90024-8.
16. O.D Sherby, J.L Lytton, J.E Dorn, Acta Metallurgica **5**, 219–227 (1957). https://doi.org/10.1016/0001-6160(57)90169-4.
17. R. Fernández, G. González-Doncel, J. Alloys and Comp. **440**, 158–167 (2007). https://doi.org/10.1016/j.jallcom.2006.09.041.
18. O.D Sherby, J. Weertman, Acta Metallurgica **27**, 387–400 (1979). https://doi.org/10.1016/0001-6160(79)90031-2.
19. S. Spigarelli, M. Cabibbo, E. Evangelista, J. Bidulska, J. of Mat. Sci. **38**, 81–88 (2003). https://doi.org/10.1023/A:1021161715742.
20. F. Bardi, M. Cabibbo, E. Evangelista, S. Spigarelli, M. Vukcevic, Mat. Sci. Eng. A **339**, 43–52 (2003). https://doi.org/10.1016/S0921-5093(02)00103-X.
21. M.J. Styles, R.K.W. Marceau, T.J. Bastow , H.E.A. Brand, M.A. Gibson, C.R. Hutchinson, Acta Mater. **98**, 64–80 (2015). https://doi.org/10.1016/j.actamat.2015.07.011.
22. R.K.W. Marceau, C. Qiu, S.P. Ringer, C.R. Hutchinson, Mat. Sci. Eng. A **546**, 153–161 (2012). https://doi.org/10.1016/j.msea.2012.03.043.
23. M.J. Starink, Int. Mater. Rev. **49**, 191–226 (2004). https://doi.org/10.1179/095066004225010532.
24. Y.C. Lin, Yu.Chi Xia, Yu.Qiang Jiang, Lei.Ting Li, Mat. Sci. Eng. A **556**, 796–800 (2012). https://doi.org/10.1016/j.msea.2012.07.069.
25. G.D. Bokuchava, A.M. Balagurov, I.V. Papushkin et al., J. of Surf. Invest. X-ray, Synch. and Neut. Tech. **4**(*6*), 879–890 (2010). http://doi.org/10.1134/S1027451010060029.
26. G.D. Bokuchava, V.L. Aksenov, A.M. Balagurov et al., Appl. Phys. A: Mat. Sci. & Proc **74** (*Suppl1*), s86–s88 (2002). http://doi.org/10.1007/s003390201750.
27. G.D. Bokuchava, I.V. Papushkin et al., Rom. J. Phys. **61**(*3–4*), 491–505 (2016). http://www.nipne.ro/rjp/2016_61_3-4/0491_0505.pdf.
28. P. Hiismäki, H. Pöyry, A. Tiitta, J. of Appl. Cryst. **21**, 349–354 (1988). http://doi.org/10.1107/S0021889888003024.
29. A.M. Balagurov, I.A. Bobrikov, G.D. Bokuchava et al., Particles & Nuclei **46**(*3*), 249–276 (2015). http://doi.org/10.1134/S1063779615030041.
30. Y.M. Ostanevich, Macromol. Chem. Macromol. Symp. **15**, 91 (1988).
31. G.D. Bokuchava, I.V. Papushkin, V.I. Bobrovskii, N.V. Kataeva, J. of Surf. Invest. X-ray, Synch. and Neut. Tech. **9**(*1*), 44–52 (2015). http://doi.org/10.1134/S1027451015010048.
32. A.M. Balagurov, I.A. Bobrikov, G.D. Bokuchava et al., Mat. Charact. **109**, 173–180 (2015). http://doi.org/10.1016/j.matchar.2015.09.025.
33. G.D. Bokuchava, Rom. J. Phys. **61**(*5–6*), 903–925 (2016). http://www.nipne.ro/rjp/2016_61_5-6/0903_0925.pdf.
34. H.M. Rietveld, J. Appl. Cryst. **2**, 65–71 (1969). http://doi.org/10.1107/S0021889869006558.
35. G. Effenberg, A. Prince, N. Lebrun, H.L. Lukas, M.G. Harmelin, *Al-Cu-Mg (Aluminium-Copper-Magnesium): Datasheet from Landolt-Börnstein – Group IV Physical Chemistry*, Volume 11A2: "Light Metal Systems. Part 2" in Springer Materials, Springer-Verlag, Berlin Heidelberg. http://doi.org/10.1007/10915967_4.
36. Guinier, G. Fournet, *Small Angle X-ray Scattering*, John Wiley, New York, 1955. http://doi.org/10.1002/pol.1956.120199326.
37. C.S.T. Chang, F. De Geuser, J. Banhart, J. Appl. Cryst. **48**, 455–463 (2015). http://doi.org/10.1107/S1600576715002770.
38. M. Doucet et al. SasView Version 4.1, Zenodo, https://doi.org/10.5281/zenodo.438138.
39. P. Donnadieu, F. Carsughi, A. Redjaimia et al., J. Appl. Cryst. **31**, 212–222 (1998). http://doi.org/10.1107/S002188989701011X.
40. Cheng-Si Tsao, E-Wen Huang, Ming-Hsien Wen, et al., J. Alloy. Comp. **579**, 138–146 (2013). http://doi.org/10.1016/j.jallcom.2013.04.201.